Catalysis Science & Technology

Accepted Manuscript

This article can be cited before page numbers have been issued, to do this please use: M. A. Rodriguez Olguin, N. Herbert, H. Atia, M. Bosco, E. L. Fornero, R. Eckelt, D. A. De Haro-Del Rio, A. Aguirre, H. J.G.E. Gardeniers and A. Susarrey-Arce, *Catal. Sci. Technol.*, 2022, DOI: 10.1039/D2CY00143H.

ROYAL SOCIETY OF CHEMISTRY

rsc.li/catalysis

View Article Online
DOI: 10.1039/D2CY00143H

Tunning catalytic acidity in Al_2O_3 nanofibers with mordenite nanocrystals for dehydration reactions

M.A. Rodriguez-Olguin[1,#], R. N. Cruz-Herbert[2,#], H. Atia[3], M. Bosco[4,5], E.L. Fornero[4,6], R. Eckelt[3], D. A. De Haro Del Río[2,], A. Aguirre[4,*], J.G.E. Gardeniers[1,*], A. Susarrey-Arce[1,*]*

[1]Mesoscale Chemical Systems, MESA+ Institute, University of Twente, PO. Box 217, 7500AE, Enschede, The Netherlands

[2]Universidad Autónoma de Nuevo León, Facultad de Ciencias Químicas, Pedro de Alba S/N., San Nicolás de los Garza, Nuevo León, 64455, México

[3]Leibniz Institute for Catalysis, Albert-Einstein-Straße 29a, D-18059, Rostock, Germany

[4]Instituto de Desarrollo Tecnológico para la Industria Química (INTEC), Universidad Nacional del Litoral, CONICET, Güemes 3450, S3000GLN, Santa Fe, Argentina

[5]Facultad de Ingeniería Química, Universidad Nacional del Litoral (UNL), Santiago del Estero 2829, Santa Fe, 3000, Argentina

[6]Facultad de Ingeniería en Ciencias Hídricas, UNL, Ciudad Universitaria. Ruta Nacional N° 168 - Km 472,4, 3000 Santa Fe, Argentina.

[#]These authors contributed equally to this work

Corresponding authors: A. Aguirre (aaguirre@santafe-conicet.gov.ar); D. A. De Haro Del Río (david.dharodlr@uanl.edu.mx); J.G.E. Gardeniers (j.g.e.gardeniers@utwente.nl); A. Susarrey-Arce (a.susarreyarce@utwente.nl)

View Article Online
DOI: 10.1039/D2CY00143H

Abstract

Alumina (Al_2O_3) is one of the most used supports in the chemical industry due to its exceptional thermal stability, surface area, and acidic properties. Mesoscopic structured alumina with adequate acidic properties is important in catalysis to enhance selectivity and conversion of certain reactions and processes. This study introduces a synthetic method based on electrospinning to produce Al_2O_3 nanofibers (ANFs) with zeolite mordenite (MOR) nanocrystals (hereafter, hybrid ANFs) to tune the textural and surface acidity properties. The hybrid ANFs with electrospinning form a non-woven network with macropores. ANF-HMOR, i.e., ANFs containing protonated mordenite (HMOR), shows the highest total acidity of ca. 276 µmol/g as determined with infrared spectroscopy using pyridine as a molecular probe (IR-Py). IR-Py results reveal that Lewis acid sites are prominently present in the hybrid ANFs. Brønsted acid sites are also observed in the hybrid ANFs and are associated with HMOR presence. The hybrid ANFs functionality is evaluated during the methanol dehydration to dimethyl ether (DME). The proof of concept reaction reveals that ANF-HMOR is the more active and selective catalyst with 87% conversion and nearly 100% selectivity to DME at 573 K. The results demonstrate that the textural properties and the acid site type and content can be modulated in hybrid ANF structures, end-synergistically improving selectivity and conversion during the methanol dehydration reaction. From a broader perspective, our results promote the utilization of hybrid structural materials as a means to tune chemical reactions selectively.

Keywords: electrospinning, Al_2O_3, nanofibers, mordenite, acidity, methanol dehydration, DME

View Article Online
DOI: 10.1039/D2CY00143H

Introduction

Al_2O_3 in heterogeneous catalysis has been used to support alkali metals, noble metals, and metal oxides with a wide range of applications in biomass upgrading, oil industry, and automotive sector.[1–8] Such a wide range of applications is due to the various Al_2O_3 polymorphs,[9,10] each with unique properties, such as thermal stability, acidity, and high specific surface area, targeted for specific reactions.[11–16] Besides the current synthetic approaches in Al_2O_3,[16–24] structuring of mesoscopic scale Al_2O_3 remains a challenge. Typical methods to structure Al_2O_3 are extrusion[8], injection molding,[25] and 3D printing.[25,26] These methods search to improve reaction rates via mass transfer and diffusivity varying the Al_2O_3 geometries. Although such Al_2O_3 structures are often relevant in catalysis, sufficient attention should be paid to the chemical properties of Al_2O_3, such as the nature of the acid sites to promote acidity in structural acid catalysts.

Electrospinning is a convenient method that provides sufficient versatility to optimize chemical properties in structured materials.[27–36] The method produces nanofiber-like structures formed during the withdrawal of a jet from a droplet subjected to an external electric field, which later is deposited over a collector plate for further treatment.[37–39] Although the approach has been primarily used in the biomedical field,[40] it is increasingly used for energy storage, energy conversion, and catalysis.[41,42,43] In the past, ceramic materials, including alumina, have been subject to modifications that have led them to have one-dimensional (1-D) configurations, such as nanofibers.[44] These arrangements have attracted attention due to the unique functionality provided by nanofibers. For example, high mechanical strength, high surface-area/weight ratio, chemical composition, and stability.[44,45,46] Recently, M.A. Rodriguez-Olguin et al.[43] demonstrated that acid site content can be enhanced in ANFs. The authors use various aluminum precursors during electrospinning. From the precursor assessment, Aluminum Di(sec-butoxide)acetoacetic Ester Chelate (ASB) is identified as the ideal precursor to obtaining ANFs with a large amount of weak and medium strength Lewis acid sites (LAS).

View Article Online
DOI: 10.1039/D2CY00143H

Furthermore, ASB chelate promotes mesopores of 2-50 nm in size.[47–51] Macropores (i.e. >50 nm), especially relevant in catalysts, can also be observed between the fiber-to-fiber interspaces.[43] From this perspective, it is fair to say that the benefit of nanofibers relies on its hierarchy having multiple levels of porosity that combine meso-/macro-pores.

Similarly, multilevel porosity can be found in hierarchical catalysts, such as zeolites. Zeolite has pore sizes ranging from micropores to mesopores and macropores.[52,53,54] These pores are composed of Si and Al atoms coordinated with oxygen, forming channel networks of diverse sizes. However, if the zeolite pores are too small, the reaction might be diffusion or mass transport limited. Synthetic methods to increase the meso-/macropores availability have been established to reduce transport issues. A widely applied approach in zeolites is leaching.[55] However, leaching involves several synthetic steps that are composition and zeolite type dependent. An interesting alternative is providing structure to existing catalysts, such as zeolites. Zeolites are compatible with synthetic approaches, such as electrospinning.[56–62] A key aspect of electrospinning is that it can facilitate the formation of macropores without limiting mesopore formation.[43]

Reports have demonstrated advantages for shaped zeolites as either single or hollow nanofiber.[56,57] This includes crystalline fibers of zeolite Y,[58,59] ZSM-5,[60,61] and SUZ-4.[62] Other approaches used to structure zeolites involve templates or zeolite mixtures with more materials to create composites. For example, F. Ocampo et al.[63] developed a multimodal pore size distribution using a zeolite and a glass monolith. The authors demonstrate the HZSM-5/glass monolith functionality during n-hexane cracking. Following a similar concept, zeolite Y, MFI, or Beta on α-SiC foams, carbon nanotubes, or TiO_2 nanofibers have been synthesized and tested during a catalytic reaction.[64,65,66] From the previous examples, MOR shaped as nanofibers or MOR composites within a nanofiber are limited but increasingly recognized as an effective way

View Article Online
DOI: 10.1039/D2CY00143H

to enhance conversion and selectivity in chemical reactions, such as CO_2 methanation using a silica MOR composite.[67]

The rationale behind using MOR in structured materials as composite is to find more dimensionally refined systems that allow easy access to molecules to adsorb, react and desorb over LAS and Brønsted acid sites (BAS).[68] This is the case for acid catalysts, widely used for alcohol dehydration reactions, such as methanol dehydration to DME.[69,70] An accepted mechanism for the mentioned reaction occurs with the adsorption of the alcohols over a LAS or BAS, and an adjacent LAS forming two species, which produce DME and water upon condensation.[71] However, in this reaction, a tradeoff between the LAS and BAS strength has to be found because it can significantly alter methanol dehydration products.[72] It is generally accepted that the DME synthesis preferably proceeds on a solid acid catalyst with weak and moderate acidic sites. For strong BAS commonly found in MOR,[73,74] a considerable amount of side-products can be formed. The products consist predominantly of hydrocarbons or coke, which affect the selectivity and lifespan of the catalyst. An alternative that can compensate for high BAS contents is a composite, for example, MOR with Al_2O_3 shaped as nanofiber.[75] Al_2O_3[76–81] is a known catalyst used to dehydrate methanol and produce DME by following a proposed mechanism based purely on LAS.[82,83] From this perspective, a synergy between acid catalysts containing LAS and BAS has to be found to tune chemical reactions like DME selectively.

The present work synthesized nanofibers composed of amorphous Al_2O_3 and MOR with electrospinning. The synergy of MOR and amorphous Al_2O_3 is demonstrated by comparing the hybrid ANFs with Al_2O_3 shaped as nanofiber. The added value of the structured fibers is assessed by comparing hybrid ANFs against Al_2O_3 and MOR without nanofiber shape. Structural and morphological analysis indicates the presence of MOR in the ANFs. Textural analysis corroborates our findings, where a decrease in the surface area for hybrid fibers is

observed. Furthermore, hybrid ANFs show the highest acidity as determined with IR-Py. The acid sites present in the hybrid ANFs are LAS and BAS, while for the control samples of Al_2O_3, only LAS has been found. The hybrid ANFs functionality is assessed during methanol dehydration to DME as a proof of concept reaction. The results reveal a synergetic effect between Al_2O_3 and MOR in the nanofibers and demonstrate the added value of hybrid materials in chemical reactions.

View Article Online
DOI: 10.1039/D2CY00143H

Methodology

Microwave-assisted zeolite synthesis

Microwave-assisted hydrothermal synthesis was carried out to produce NaMOR nanocrystals. Colloidal silica (Ludox HS-40, 40% w/w, Aldrich), $Al(OH)_3$ (98%, Aldrich), and NaOH (98%, Sigma-Aldrich) were used as precursors to obtain an initial gel with the ratio 6 NaOH: Al_2O_3:30 SiO_2: 780 H_2O. In a typical run, 1.6 g of $Al(OH)_3$ were dissolved in 2.2 g of NaOH (98%, Sigma-Aldrich) and 61 g of deionized water. Then, 11.4 g of colloidal silica were added until complete dissolution, and 3g of MOR nanocrystals from Zeolyst were used as seeds to enhance the crystallization rate. The resulting suspension was stirred for 1 h at 450 rpm. After, the obtained gel was placed in a Teflon autoclave belonging to the Milestone Flexiwave microwave. The crystallization conditions followed a ramp of 20 K/min to reach 453 K and used 600 W as maximum power for the synthesis time (1 h). This strategy allows the reduction of the synthesis time that has traditionally been reported from 24-48 h. Finally, the material was recovered by filtration, washed to a pH lower than 9, and dried at 343 K for 24 h in air. The final Si/Al ratio as determined with EDX is 10.5 for all NaMOR, which are then used during the ionic exchange (see below).

Protonation of zeolite mordenite

The protonation of the NaMOR nanocrystals follows a post-treatment using 1 M NH_4NO_3 (ACS grade, Sigma Aldrich) solution in deionized water. First, NaMOR nanocrystals were dispersed in the NH_4NO_3 solution, 1 g of solid per 10 ml of solution, and stirred at 353 K for 2 h. Then, the material was washed and filtered once the time had elapsed. The product obtained was placed in the oven for 12 h, and once the time finished, the ion exchange was repeated 3 times. At the end of the ion exchanges, the samples were calcined at 773 K for 3 h in air. The material obtained was labeled as HMOR.

View Article Online
DOI: 10.1039/D2CY00143H

Hybrid fibers synthesis

The hybrid ANFs containing either NaMOR or HMOR were prepared by electrospinning using a commercial electrospinning system from IME Technologies (The Netherlands). The IME system was operated utilizing a stainless-steel needle of 0.4 mm inner diameter at a separation distance of 12 cm from the aluminum collector plate. First, a mixture consisting of 4 %p/v $C_{14}H_{27}AlO_5$ (ASB) technical grade from Alpha Aesar, 6 %p/v polyvinylpyrrolidone (PVP, MW ~1,300,000), and 0.26 %p/v t-octylphenoxypolyethoxyethanol (Triton x100, Sigma-Aldrich) dissolved in ethanol (100% Tech. grade, BOOM B.V., The Netherlands) was used as the aluminum precursor solution to generate ANFs. To make the hybrid ANFs, the synthesized NaMOR, or HMOR nanocrystals, were incorporated into the ASB solution, reaching a final concentration of 0.33 %p/v in each case. The prepared solutions were electrospun at environmental temperature and humidity using a potential of 18 kV and at an 8 mL/h infusion rate. After fiber deposition, all-fiber samples were dried in an oven at 353 K for 12 h to remove the excess solvent. Subsequently, they were calcined (Nabertherm LH 15/12) in air with a temperature ramp of 0.5 K/min to 623 K for 3 h and then 1 K/min until reaching 773 K for 4 h to ensure the production of amorphous alumina.[43] Hereafter, the obtained hybrid ANFs are named ANF-NaMOR and ANF-HMOR for simplicity. It should be noted that commercial MOR (CBV 10A, Zeolyst) was also used following the previously described hybrid nanofiber preparation. Control samples of particulate alumina (Al_2O_3-NP) and particulate alumina containing HMOR (Al_2O_3-HMOR-NP) were prepared by drop-casting using the same ASB, NaMOR, HMOR precursor solutions in crucibles. These samples were annealed following the same procedure as ANF-NaMOR and ANF-HMOR samples.

Characterization

Morphological characterization

View Article Online
DOI: 10.1039/D2CY00143H

High-resolution (HR)-SEM images of samples were taken using a Zeiss MERLIN SEM microscope operated at 1.40 kV coupled with High-Efficiency Secondary Electron Detector (HE-SE2). SEM-scanning transmission electron microscope (STEM) was recorded at 20kV. Prior to STEM analysis, samples were sonicated in ethanol, which led to the fragmentation of the fibers into smaller fiber pieces.

Structural characterization

The crystalline structure of NaMOR and HMOR nanocrystals was analyzed by a Siemens (D5000, E04-0012 series) diffractometer, using CuKα radiation (λ = 1.5418 Å) operated at 35 kV, 25 mA, in the 2θ range between 5-50°, employing a step size of 0.02°/min and step time of 4 s. The hybrid fibers were analyzed by X-ray powder diffraction (D2 PHASER, Bruker) using Cu Kα radiation (λ = 1.5418 Å) operated at 30 kV, 10mA, in the 2θ range between 7-45°, employing a step size of 0.05° and a scan speed of 0.1°/s. A Si low background sample holder (Bruker) was used for the hybrid samples.

Chemical characterization

X-ray photoelectron spectroscopy (XPS) general survey analysis was performed in a Quantera SXM machine from Physical Electronics using monochromated Al Kα (1486.6 eV). All samples were fixed in a stainless-steel holder. Low energy electron flood gun was used to supply the missing photo- and Auger electrons. The electron binding energies were referenced to aliphatic carbon C 1s at 284.8 eV. The obtained peak analysis was made using the PHI Multipak V9.9.0.8 software (Physical Electronics, Inc.).

Textural analysis

BET surface area, pore-volume, and pore diameter of the samples were determined from the nitrogen adsorption/desorption isotherms at 77K on a Micrometrics ASAP 2010 instrument.

View Article Online
DOI: 10.1039/D2CY00143H

Before the measurement, each sample was evacuated at 473K for 4 h. The pore size distributions were calculated from the desorption branch of the isotherm using the Barrett-Joyner-Halenda (BJH) model.[54]

NH_3-TPD

To determine the total acidity properties of the samples, NH_3-TPD analysis was performed using a Micromeritics Autochem II 2910 instrument. Prior to NH_3 adsorption, 150 mg of the sample was loaded into a U-shaped quartz reactor and heated from RT to 673 K with 10 K/min in a flow of He (50 ml/min), held for 30 min at 673 K (to remove any adsorbed species on the surface). After that, the reactor was cooled to 373K. The sample was saturated with 1% NH_3 in He (50 ml/min) for 120 min at 373 K, followed by helium flushing (50 ml/min) for 60 min at 373 K to remove physisorbed NH_3. The sample was then heated to 1073 K at a rate of 10 K/min in He flowed (50 mL/min) and held at 1073K for 30 min for NH_3 desorption. The effluent gasses were analyzed with a Quadrupole mass spectrometer (Balzers Omnistar) using m/z = 15.

IR measurements and Pyridine adsorption

The nature and strength of acid sites were determined through pyridine (Py) adsorption over the materials and subsequent temperature-programmed desorption (TPD-Py). The samples were analyzed with IR spectroscopy through in situ transmission on self-supported wafers (10-15 mg, 13 mm of diameter) pressed at 5 t cm^{-2} (490 MPa). The wafers were placed in a Pyrex IR cell fitted with water-cooled NaCl windows. More details of the experimental setup can be found elsewhere.[84] Before the adsorption experiments, each sample was pretreated in situ at 723K (10 K/min) for 30 min under N_2 flow (50 sccm), then cooled down to 303K, and the reference IR spectra of the "clean wafer" were taken. The samples were exposed to a flow of N_2 containing evaporated Py. The physisorbed Py was further removed under flowing N_2 until the spectra of the adsorbed Py remained stable (about 60 min). The thermal desorption of Py

View Article Online
DOI: 10.1039/D2CY00143H

was measured from 303K to 723K with 5 K/min in a flow of N_2 (50 ml/min). The spectra were acquired with a Nicolet Magna 550 FTIR spectrometer with a cryogenic MCT detector (4 cm^{-1} resolution, 25 scans). The gas used in this study was high purity grade N_2 (INDURA UHP 99.999%) and was further purified through a molecular sieve (3 Å), and MnO/Al_2O_3 traps to remove water and oxygen impurities, respectively.

Catalytic test

The synthesized materials were tested for the dehydration of methanol to dimethyl ether (DME) between 423 and 723 K (heating ramp of 1K/min) in a fixed bed glass tubular microreactor (i.d. = 5.3 mm). The reactor was loaded with 50 mg of catalyst diluted (1:5) with milled quartz (200 mesh). The methanol concentration was 7% v/v in Ar obtained from a gas saturator filled with pure methanol immersed into a thermostatic bath. The total flow rate was set to 20 mL/min, giving a weight hourly space velocity (WHSV) of 2.3 $g_{methanol}/g_{cat}$ h. The pipelines were heated to prevent methanol and products condensation. Before the catalytic test, the samples were pretreated at 673 K under the flow of Ar (50 mL/min) for 1 h. The outlet gas stream was analyzed continuously with a mass spectrometer Prisma QMG220 (Pfeiffer). The following mass/charge signals were recorded: 2(H_2), 16 (CH_4), 18 (H_2O), 28 (CO), 29, 31 and 32 (methanol), 40 (Ar), 44 (CO_2), 45 (DME), 58 and 59 (olefins).

View Article Online
DOI: 10.1039/D2CY00143H

Results and discussions

Hybrid ANFs containing MOR

The synthesis of the hybrid ANFs started by selecting the MOR crystallite size. Commercial NaMOR, which has an average crystallite size of 220 nm (**Figure S1a**), has been used during electrospinning. However, it is found that this leads to severe heterogeneities after annealing (**Figure S1b)**). These heterogeneities are attributed to the relatively large (compared to the nanofiber dimensions) crystallite size of NaMOR, which upon annealing, promotes nanofiber instability leading to hybrid ANFs without shape (**Figure S1b)**). In contrast to the commercial NaMOR, the synthesized NaMOR shown in **Figure S2** has smaller crystallite sizes ranging between 110 and 118 nm. The crystallite size is nearly half of the nanofiber diameter. From the results, small MOR crystallite can lead to fewer heterogeneities in ANFs, as shown in **Figure 1**. In this Figure, the hybrid ANFs (**Figure 1c)** and **Figure 1e)**) retain their nanofiber shape, similar to ANFs in **Figure 1a)** that show a non-woven fiber morphology. The estimated nanofiber diameters are 321±74 nm for ANFs, 315±120 nm for ANFs containing NaMOR (ANF-NaMOR), and 241±76 nm for ANFs containing HMOR (ANF-HMOR).

A detailed structural analysis using dark-field STEM images is also presented in **Figures 1b), 1d),** and **1f)** to provide insights into the hybrid ANFs morphology. From the images, less dense ANFs nanofibers are found in **Figure 1b)**. The effect becomes evident at the edges of the ANFs, with small pore openings (see yellow arrows). In contrast, STEM images of ANF-NaMOR and ANF-HMOR in **Figures 1d)** and **1f)** show denser areas at the borders and center of the fiber structure, possibly due to MOR nanocrystals inside the fibers, which could act as a 'filler' material densifying the nanofibers. It should be noted that the high amount of broken fibers is due to the sonication used during specimen preparation for STEM. To this end, EDS mapping in **Figure S3** is used to verify the hybrid nanofiber constitution and generate insights into the

View Article Online
DOI: 10.1039/D2CY00143H

MOR distribution by looking at the silicon Kα1 signal. Silicon signal has been found in the non-woven structure and specific densified areas.

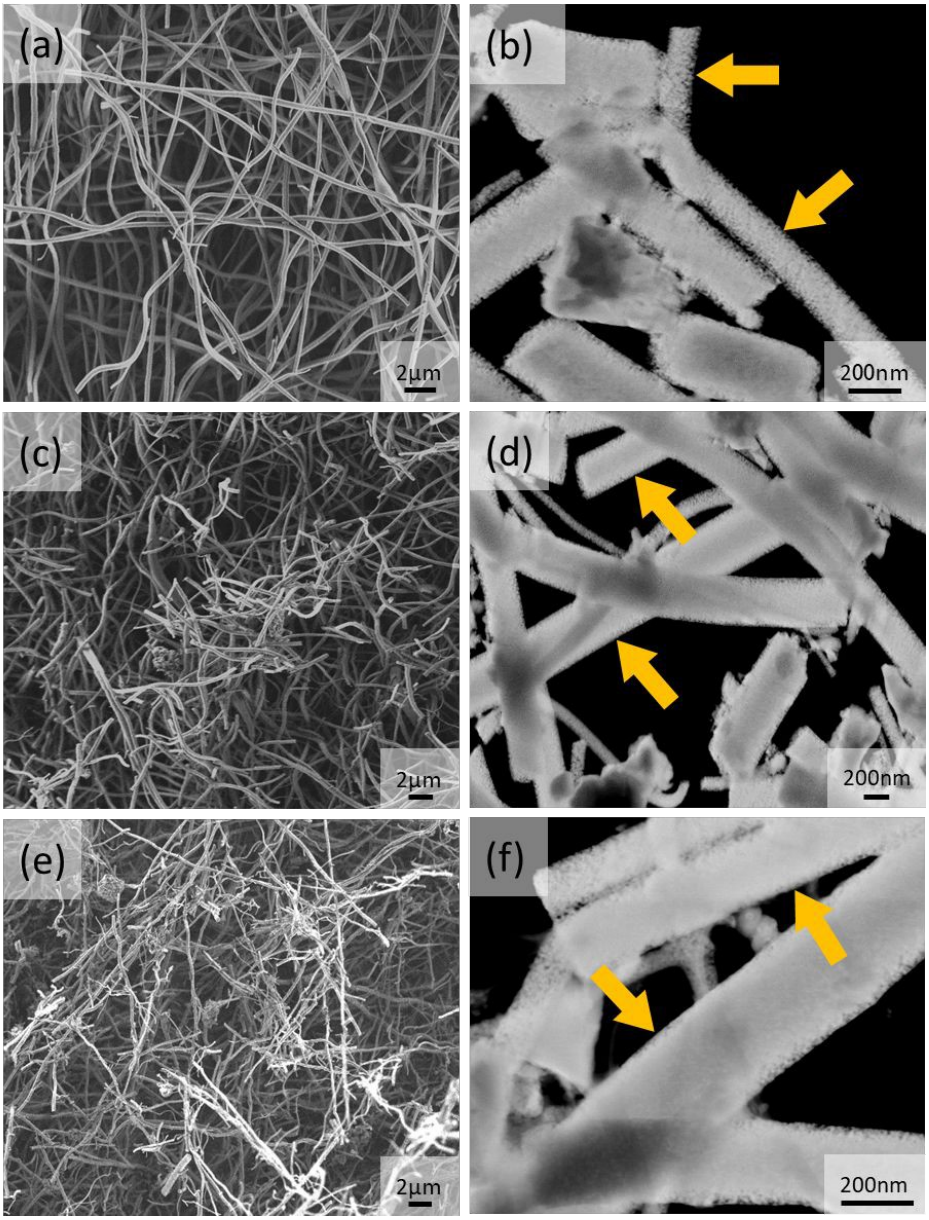

Figure 1. SEM and dark-field STEM images of (**a,b**) ANFs, (**c,d**) ANF-NaMOR and (**e,f**) ANF-HMOR. The yellow arrows highlight the pore openings in the fibers.

The chemical composition at the surface of the hybrid ANFs from **Figure 1** is analyzed with XPS to determine the types of species present on the hybrid ANFs (**Figure S4** and **Table S1**). In short, elemental analysis with XPS in **Table S1** reveals nitrogen presence in MOR. The results suggest that NH_4^+ has exchanged with NaMOR to form the acidic form of MOR after

View Article Online
DOI: 10.1039/D2CY00143H

calcination. Temperature desorption carried out for HMOR demonstrates that at 773 K, NH_4^+ could be retained at the catalyst.[85] For temperatures 823 K, the NH_4^+ in the form of NH_3 has not been detected.[85] For ANF-HMOR in **Table S1**, no nitrogen has been observed. NH_3-TPD is carried out for ANF-NaMOR and ANF-HMOR to demonstrate an increase in acidity in ANF-HMOR, most probably from the HMOR. In this case, ANF-NaMOR is used as a control. ANF-NaMOR show 112 μmol/g of NH_3 desorbed, whereas ANF-HMOR has 216 μmol/g of NH_3 desorbed. The general survey of the nanofibers revealed only the presence of aluminum and oxygen. Therefore, we can ensure that neither the ANFs nor hybrid fibers contain impurities from the electrospinning precursors. Additionally, to verify the MOR content in ANFs, XRD is assessed. The XRD diffraction patterns of NaMOR and HMOR nanocrystals and the hybrid ANFs are presented in **Figure 2**. First, we investigate the crystallographic features of the NaMOR before and after ion exchange with NH_4^+. The XRD diffraction patterns of NaMOR and HMOR are presented in **Figure 2a).** The XRD for NaMOR shows diffraction peaks at 2θ = 9.8° (200), 13.5° (111), 19.7° (330), 22.3° (150), 25.7° (202), 26.4° (350), 27.7° (511), 31.0° (402) which match with literature from MOR (2θ = 9.8°, 13.5°, 19.6°, 22.3°, 25.7°, 26.3°, 27.5°, and 30.9°).[86–88] HMOR present similar diffraction peaks as NaMOR (2θ = 9.8°, 13.5°, 19.7°, 22.4°, 25.7°, 26.4°, 27.7°, and 31°). No other crystallographic phase is observed for both samples. **Figure 2b)** compares the HMOR nanocrystals with ANF-NaMOR and ANF-HMOR hybrid fibers. In the same **Figure 2b)**, XRD of nanofibers is presented. No crystalline phase has been observed for the ANF sample, confirming the amorphous characteristic of ANF. ANF-NaMOR and ANF-HMOR diffractograms present peaks that correspond to MOR (**Figure 2a)**). No other crystallographic phase for the hybrid ANFs is observed.

View Article Online
DOI: 10.1039/D2CY00143H

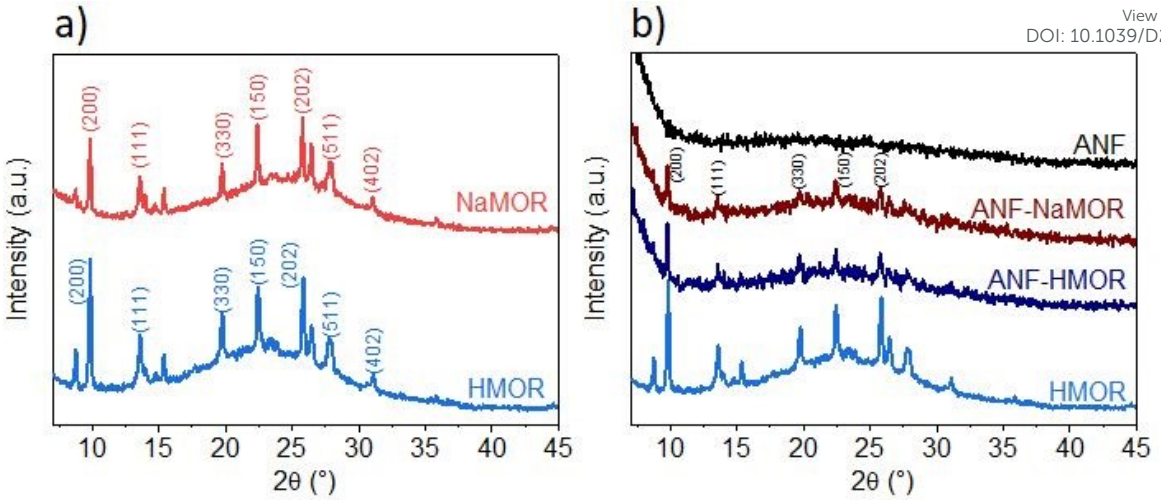

Figure 2. a) XRD diffraction pattern of bare NaMOR and HMOR nanocrystals and **b)** ANFs, ANF-NaMOR, and ANF-HMOR.

The effect of MOR has been observed in **Figure 1** with more densified hybrid nanofibers. The presence of MOR in the hybrid fibers became evident with the XRD analysis in **Figure 2**. However, an essential aspect is understanding how MOR affects the surface area in the nanofibers. In **Table 1**, the total surface area of the nanofibers is presented. From the produced catalysts, ANFs possess the highest surface area (192 m^2/g), followed by hybrid ANF-HMOR (121 m^2/g) and ANF-NaMOR (107 m^2/g). The reason for a reduced surface area for nanofibers is that the NaMOR or HMOR might block pore accessibility in ANFs.[54,89,90]

To generate insights into the pore distribution for ANFs with and without MOR, the analysis of the BET isotherms is presented in **Figure 3**. For ANFs, ANF-NaMOR, and ANF-HMOR in **Figure 3a)**, adsorption-desorption isotherms showed hysteresis loops in the multilayer step, which is associated with capillary condensation type IV isotherms for mesopores with H2 hysteresis according to IUPAC classification.[91] The hysteresis loop is characteristic of mesoporous materials with cage-like pores or pores with constrictions at the pore opening.[92,93]

The pore distribution plots are presented in **Figure 3b)** and revealed a wide distribution of pore bodies, with a majority distribution of pore widths around 6 nm for ANFs and hybrid ANFs with NaMOR and HMOR. **Figure 3b)** shows that ANFs have the highest mesopore and incremental pore volume, followed by ANF-HMOR and ANF-NaMOR. This indicates that the MOR modifies the textural properties of ANFs by decreasing the number of pore bodies. The results agree with STEM images in **Figures 1b**), **1d)**, and **1f)**.

Taking the results from the ANFs and hybrid ANFs together, the effect of structuring should be compared with the same type of catalysts but without nanofiber shape, as shown in **Figure S5**. The Al_2O_3-NP and Al_2O_3-HMOR-NP control samples have been produced using the same alumina and HMOR precursors. The total surface area of Al_2O_3-NP and Al_2O_3-HMOR-NP are presented in **Table 1**. This table shows a decrease in surface area of approximately 30 m^2/g for Al_2O_3-NP compared to the ANFs counterpart. Similar results are observed for Al_2O_3-HMOR-NP and the hybrid ANF-HMOR. We hypothesize that the ANFs are less prone to sintering due to restriction of the growth of crystals in the fibers (by confinement) and thus present a higher surface area, as shown in **Table 1**. When comparing the BET isotherms, variations between the Al_2O_3-NP or Al_2O_3-HMOR-NP are observed. In this case, the type IV adsorption-desorption isotherm shape with an H3 hysteresis loop has been found for Al_2O_3-NP and Al_2O_3-HMOR-NP (**Figure 3a)**). Here, the sharp increase at high P/P_0 (0.85-0.99) suggests the presence of

View Article Online
DOI: 10.1039/D2CY00143H

aggregated slit-shaped pores, which may originate in the interparticle voids. For isotherms with hysteresis loop at high P/P_0, it is likely to observe wide pore size distribution,[94–97] as observed in the inset in **Figure 3b)**. The pore size corresponds to Al_2O_3-NP, and Al_2O_3-HMOR-NP is 9 nm, similar to the hybrid ANFs. These results might indicate that the hybrid ANFs also provide access for the diffusion of N_2 molecules, most probably due to the fiber network.[43]

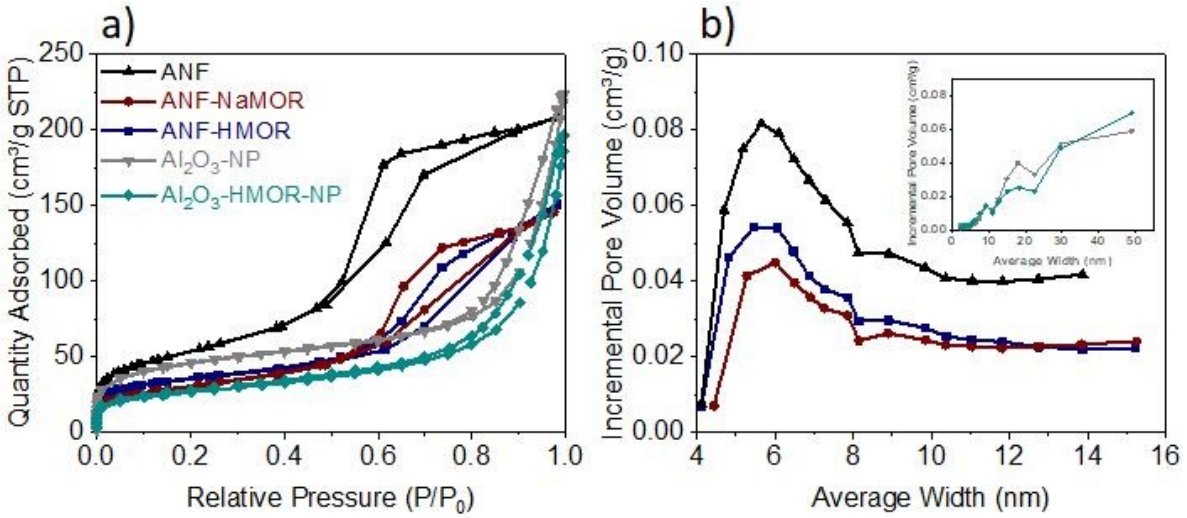

Figure 3. (a) Adsorption-desorption isotherms and (b) pore size distribution for ANFs, ANF-NaMOR, ANF-HMOR, Al_2O_3-NP, and Al_2O_3-HMOR-NP.

Table 1. Fiber diameter, surface area, pore size, and total acidity of ANFs, ANF-NaMOR, ANF-HMOR, Al_2O_3-NP, and Al_2O_3-HMOR-NP.

Sample	Surface area (m^2/g)	Total acidity at 373 K (μmol/g)	Total acidity at 373 K (μmol/ m^2)
ANFs	192	178	0.9
ANF-NaMOR	107	116	1.1
ANF-HMOR	121	276	2.3
Al_2O_3-NP	162	255	1.6

View Article Online
DOI: 10.1039/D2CY00143H

Al_2O_3-HMOR-NP	94	184	2.0

Pyridine (Py) is used as a probe molecule to determine the nature of the acid sites (i.e., either LAS or BAS).[98] In **Figures 4a)** and **4b)**, the FTIR spectra of Py adsorbed at 303 K are presented. The samples composed of alumina mainly (ANFs, Al_2O_3-NP), Al_2O_3-HMOR-NP, and hybrid alumina (ANF-NaMOR, ANF-HMOR) present an intense band at 1446, 1577, and 1614 cm^{-1}. In the case of MOR (NaMOR, HMOR) used for comparison, these peaks are weaker. These bands are attributed to Py adsorbed on LAS, produced by uncoordinated Al^{3+} or cation vacancies.[99] The signal at 1545 cm^{-1} corresponds to Py adsorbed on BAS (PyH^+) (**Figure 4b)**). Among the MOR, only HMOR shows an IR band at 1545 cm^{-1}. This band confirms that HMOR, ANF-HMOR, and Al_2O_3-HMOR-NP, contain BAS. The results help to validate the presence of HMOR in the ANFs. NaMOR and ANF-NaMOR do not reveal BAS, and thus, are not tested during DME production. Interestingly, it should be noted that for all samples, two peaks close to 1594 cm^{-1} and 1491 cm^{-1} are present and are assigned to hydrogen-bonded Py and Py adsorbed on both LAS and BAS.[100]

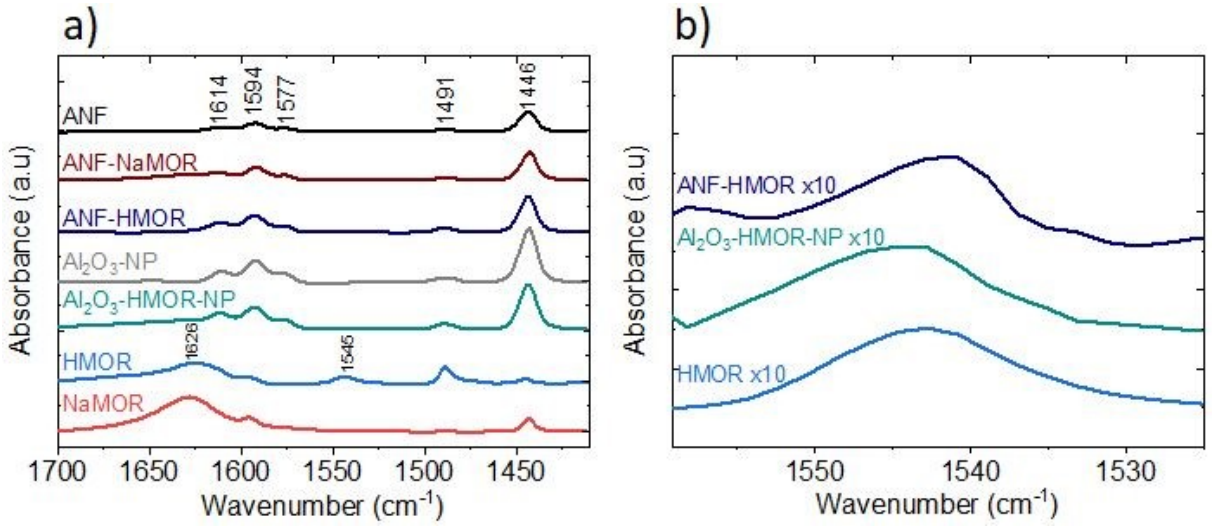

View Article Online
DOI: 10.1039/D2CY00143H

Figure 4. FTIR spectra after Py adsorption at 303 K. a) Full Py range. b) Detailed Py spectra highlighting the BAS band.

We continued with Py-TPD analysis to determine the amount and the strength of LAS and BAS from **Figure 4**. Py-TPD in **Figure 5** shows the LAS and BAS density (expressed in μmol/g) as a function of temperature, estimated using the 1446 cm^{-1} and 1545 cm^{-1} IR bands, where the band at 1446 cm^{-1} is used to estimate the total amount of LAS. Several authors[101–103] showed that the integrated molar extinction coefficients of LAS do not depend on the nature of oxides, the structure, and the strength of acid sites. Therefore, the Emeis's[101] averaged extinction coefficients of Py adsorption on LAS (2.22 cm μmol^{-1}) and BAS (1.67 cm μmol^{-1}) are used to quantify the number of sites. For BAS, the IR band at 1545 cm^{-1} is used for quantification.

View Article Online
DOI: 10.1039/D2CY00143H

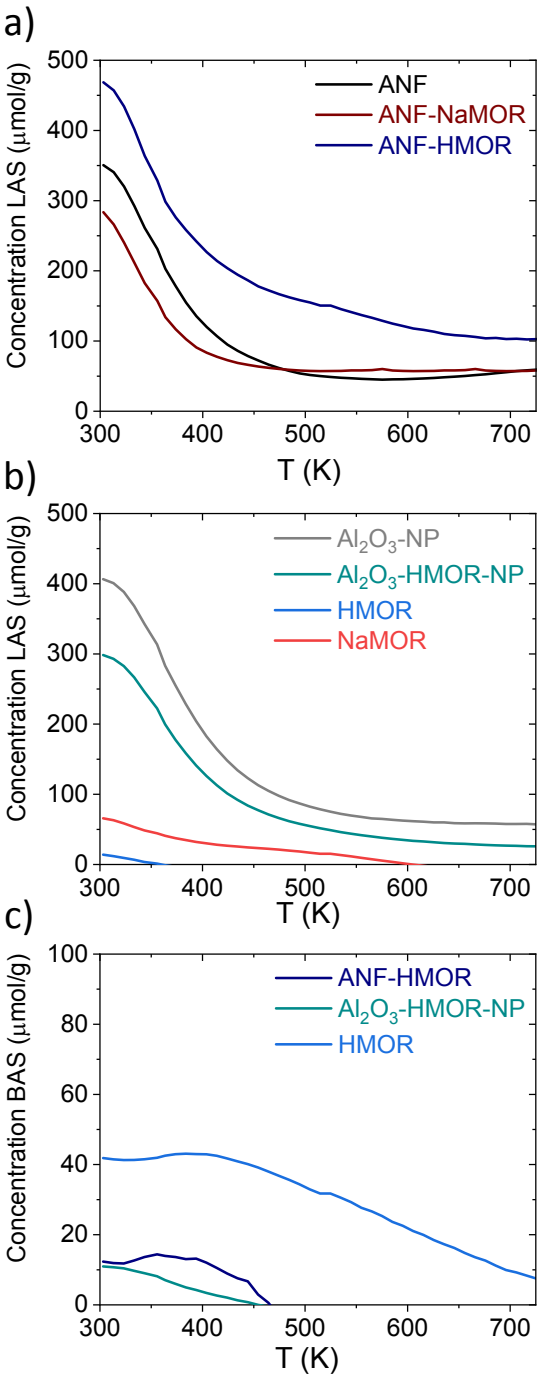

Figure 5. Py-TPD for ANF, ANF-NaMOR, ANF-HMOR, Al_2O_3-NP, Al_2O_3-HMOR-NP, HMOR, and NaMOR. In **a)**, **b)** LAS (µmol/g), and **c)** BAS (µmol/g) are shown for various samples.

From **Figure 5a)**, at 303 K, the hybrid ANF-HMOR has the highest LAS content. This can be correlated to the presence of HMOR. Contrary to ANF-HMOR, ANF-NaMOR shows the lowest LAS concentration, probably because the NaMOR blocks the acid sites of the

View Article Online
DOI: 10.1039/D2CY00143H

nanofibers. Lastly, the LAS content remains also low in ANFs. In **Figure 5a)**, the experiments demonstrate that LAS content in ANF-HMOR remains higher than Al_2O_3-NP, Al_2O_3-HMOR-NP, or MOR, as shown in **Figure 5b)**. A possible explanation for ANF-HMOR is that incorporating modifiers on alumina (e.g., HMOR) might promote dealumination, leading to the formation of multiple Al species. Along with HMOR, such Al species can increase the amount of LAS.[104,105] The results indicate that structured hybrid systems, such as ANF-HMOR can achieve high acidity, even higher than unstructured acid catalysts (**Figure 5b)**). The rationale behind our observations is that the nanofiber structure can help densify the acid sites and provide better access to molecules (such as Py), which might be challenging in unstructured acid catalysts (**Figure S5**). Furthermore, Py-TPD reveals that Py desorbs relatively fast from LAS at low temperatures (300-350 K), indicating the presence of weak acid sites (**Figure 5a)**). At temperatures higher than 350 K, a slight decrease in Py desorption, most probably to the presence of medium and strong acid sites.[43] Interestingly, after 500 K, all the alumina-modified samples retain similar LAS, except for the ANF-HMOR, where the Py is still adsorbed at 700 K, suggesting the presence of strongly adsorbed Py species over LAS. The results in **Figures 5a)** and **5b)** (also shown in **Table 1**) confirm that hybrid ANF-HMOR is the most acid catalyst (276 µmol/g), followed by ANFs (178 µmol/g) and ANF-NaMOR (116 µmol/g).

In **Figure 5c)**, HMOR presents the highest BAS density. Py starts desorbing at 400 K and remains adsorbed until 723 K, which means it has the highest Brønsted acid strength. Hybrid ANF-HMOR and Al_2O_3-HMOR-NP present less BAS density due to the lower amount of HMOR. BAS disappears at 460 K in both cases, indicating that sites have a lower BAS strength. It is essential to mention that although Py desorption occurs in **Figure 5**, the acid sites remain present and can help to catalyze reactions, such as methanol dehydration to DME.

The amount of BAS and LAS for three different temperatures (303, 373, and 423 K) from **Figure 5** are shown in **Table 2**. In **Table 2**, the ANF-HMOR has the highest acidity and LAS/BAS ratios at 303 K and 373 K, except at 423 K. At 423 K, BAS content is slightly high for ANF-HMOR (9 µmol/g) and reflected in **Table 2**. Overall, **Figure 5** shows that incorporating MOR in the alumina modulates the acid site amount and nature.

Table 2. Calculated LAS, BAS, total acidity (µmol/g), and LAS/BAS ratios samples at various selected temperatures.

T	303K				373K				423K			
Sample	**LAS**	**BAS**	**Total acidity**	**LAS/BAS**	**LAS**	**BAS**	**Total acidity**	**LAS/BAS**	**LAS**	**BAS**	**Total acidity**	**LAS/BAS**
ANFs	351	-	351	-	178	-	178	-	95	-	95	-
ANF-NaMOR	283	-	283	-	117	-	117	-	73	-	73	-
ANF-HMOR	469	12	481	38	276	14	290	20	204	9	213	23
Al_2O_3-NP	406	-	406	-	255	-	255	-	148	-	148	-
Al_2O_3-HMOR-NP	298	11	309	27	178	6	184	30	101	2	103	49
HMOR	14	42	56	0.33	-	43	43	-	-	42	42	-
NaMOR	66	-	66	-	37	-	37	-	27	-	27	-

Methanol dehydration to DME

The methanol dehydration to DME is assessed as a proof of concept reaction to underline the functionality of the hybrid nanofibers. **Figure 6a)** shows the methanol conversion of ANF, ANF-HMOR, Al_2O_3-NP, Al_2O_3-HMOR-NP, and HMOR over a temperature range of 423 and 673 K. From these catalysts, HMOR starts converting the methanol at lower temperatures (<423 K) than Al_2O_3-NP and ANFs. However, for temperatures higher than 523 K, the alumina materials are very active and reach the equilibrium conversion at ca. 613 K (Al_2O_3-NP) and 648 K (ANFs). At 673 K, ca. 38% of conversion is reached for HMOR, while for Al_2O_3-NP and ANFs, the conversion is ca. 90%. Note that the measured conversion corresponds to the equilibrium conversion. The low conversion of HMOR can be related to the low amount of acid sites over the explored temperature range shown in **Figure 5** and **Figure 6a)**.

View Article Online
DOI: 10.1039/D2CY00143H

A comparison between Al_2O_3-NP and ANFs is also assessed. Al_2O_3-NP is more active than the ANFs, probably due to the higher amount of acid sites per weight of catalysts. Interestingly, the hybrid ANF-HMOR is more active than the Al_2O_3-NP and ANFs. This includes the light-off curves of ANF-HMOR and Al_2O_3-HMOR-NP, which are very similar. Such similarities include the methanol conversion temperature, which starts at 473 K and reaches the equilibrium conversion at ca. 598 K. However, variations in DME signal intensity are observed in **Figure 6b)** for ANF-HMOR and Al_2O_3-HMOR-NP. In this case, the results indicate that ANF-HMOR is more selective (**Table 3**) to DME than the other acid catalysts.

It is then important to compare conversion (**Figure 6a)**) and selectivity (**Table 3**) at 573K for ANF, ANF-HMOR, Al_2O_3-NP, Al_2O_3-HMOR-NP, and HMOR. ANF-HMOR remains the highest in **Figure 6a)** and **Table 3**, followed by Al_2O_3-HMOR-NP, ANFs Al_2O_3-HMOR-NP, Al_2O_3-NP, and HMOR. The temperature at 50% conversion (T_{50}) and DME selectivity are also shown in the same table. Again, ANF-HMOR remains with the lowest T_{50}, highest conversion at 573 K, and DME selectivity, followed by less selective acid catalysts such as Al_2O_3-HMOR-NP, ANFs, and Al_2O_3-NP. Interestingly, despite its lower conversion (**Figure 6a)**), the ANFs are more selective to DME than the Al_2O_3-NP (**Table 3**), most probably due to the open structure network and the high surface area among the acid catalyst in **Table 1**. Furthermore, the apparent activation energy calculated from the rate of DME production vs. 1/T is shown in **Table 3** to compare the catalyst performance further. The activation energy for the ANFs, with (99 kJ/mol) and without (96 kJ/mol) HMOR present slightly lower values than the Al_2O_3-NP (108 and 110 kJ/mol). Our results show similar values to other catalysts in the literature. This entails conversion, selectivity, and activation energy.[69,81,106]

View Article Online
DOI: 10.1039/D2CY00143H

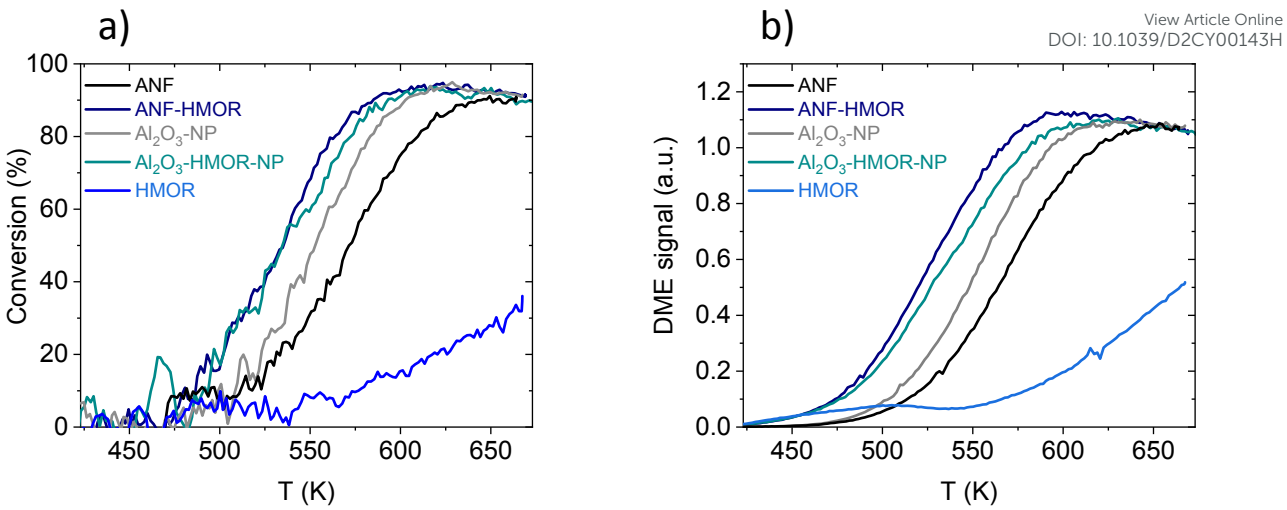

Figure 6. a) Methanol conversion during the light off curves. **b)** DME signal intensity during the light-off curves.

Table 3. Methanol conversion (%) and DME selectivity.

Sample	Methanol conversion (%) at 573 K*	DME Selectivity (relative intensity) at 573 K*	Conversion at T_{50} (K)*	DME Selectivity (relative intensity) at T_{50} (K)*	Apparent activation Energy (kJ/mol)
ANFs	46	1	573	0.9	96 ± 1
ANF-HMOR	87	1	534	1	99 ± 3
Al_2O_3-NP	72	0.9	553	0.8	110 ± 1
Al_2O_3-HMOR-NP	80	0.9	535	0.8	108 ± 4
HMOR	10	0.9	>673	-	84 ± 4

*The results are derived from the light-off curve, where the experimental error is lower than 15%.

We then compare the acidity (**Figure 5** and **Table 2**) with the catalytic performance (**Figure 6** and **Table 3**) to generate insights into the ANF-HMOR synergy. It is generally accepted that the catalyst composition, surface area, porosity (i.e., pore size and its distribution), and surface acidity affect the performance of the methanol dehydration reaction to DME.[70] In this reaction, the catalytic activity depends on the surface acidic properties, such as the total number of acidic sites and their strength. **Figure S6** shows the number of acid sites (μmol/g) and the T_{50} (K) as a function of the surface area (m^2/g). Here, it is observed that the acid sites do not depend on

View Article Online
DOI: 10.1039/D2CY00143H

the surface area, and it also does not directly influence the catalyst activity. Earlier reports[70,107] showed that the catalytic activity could be correlated with the number of acidic sites; however, this behavior has not been observed but provides insight into other factors affecting activity.[75]

From the mechanistic point, methanol dehydration is considered a bimolecular reaction between two intermediates adsorbed on adjacent surface sites and requires the proximity of two acid sites with adequate acidity.[81] Thus, increasing the acid sites density leads to improved catalyst performance. This becomes evident in **Figure 7**, which shows that the conversion increases with the acid sites density (μmol/m^2). The synergy between LAS and BAS produced by interfacial interaction also enhances the methanol dehydration rate.[108] Therefore, the addition of HMOR in the ANF and Al_2O_3-NP modifies both the acid site density and the acid types by incorporating BAS, thus improving the catalyst performance.

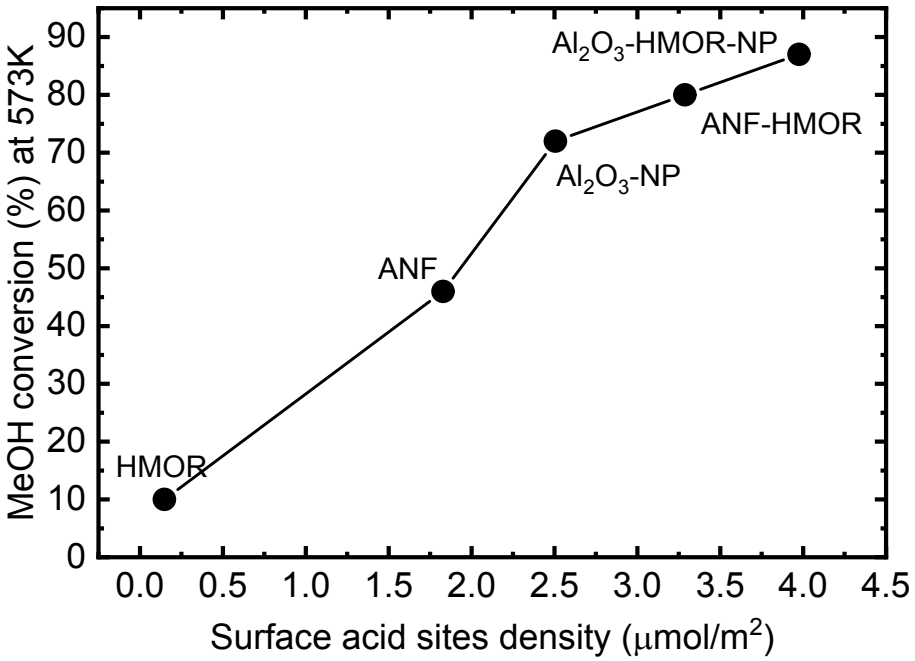

Figure 7. Conversion at 573 K as a function of the acid sites density (μmol/m^2) at 303 K for the unstructured catalysts (HMOR, Al_2O_3-NP, and Al_2O_3-HMOR-NP) and nanofibers (ANF, and ANF-HMOR).

View Article Online
DOI: 10.1039/D2CY00143H

458 In addition to the nature and strength of the acid sites, the textural properties, such as the surface
459 area, porosity, and average pore diameter, can affect the catalytic performance in dehydration
460 reactions.[69,81] The BET isotherms (**Figure 3b**) suggest the presence of aggregated slit-shaped
461 pores, which may originate in the interparticle voids in the Al_2O_3-NP and Al_2O_3-HMOR-NP.
462 Additionally, they present a wide pore size distribution. On the contrary, the pore distribution
463 plots revealed a wide distribution of pore bodies, with a majority distribution of pore widths
464 around 6 nm for ANFs and hybrid ANFs with NaMOR and HMOR. Furthermore, compared to
465 the NP that forms agglomerates and lacks structured macroporosity (**Figure S5**), the nanofibers
466 present a lower diffusion length (d=240-320 nm). This is expected due to the non-woven
467 nanofiber structure that contains macropore mesh.[43] These differences in the average pore size,
468 pore size distribution, and diffusion length may explain the variations in selectivity. In the
469 Al_2O_3-NP and Al_2O_3-HMOR-NP, the products could have a higher retention time leading to
470 by-products, such as CO and hydrocarbons, and thus decreasing the DME selectivity. Our
471 results suggest that hierarchical structures like fibers and HMOR can enhance chemical reaction
472 selectivity synergistically.

473 Based on the catalytic tests used to highlight the hybrid nanofibers' functionality, we can
474 conclude that a higher conversion of methanol to DME is achieved when samples contain high
475 acid sites densities and both types of acid sites (LAS and BAS). The presence of both types of
476 acid sites provides synergy effects that positively influence the activity towards the methanol
477 dehydration to DME. Additionally, the fiber morphology favors the DME selectivity. Further

View Article Online
DOI: 10.1039/D2CY00143H

studies on ANF-HMOR materials could optimize the amount of BAS and LAS to maximize conversion and selectivity under dehydration reactions conditions.

View Article Online
DOI: 10.1039/D2CY00143H

Conclusions

Hybrid ANFs with high acidity has been synthesized using electrospinning. Acid sites tunability is possible in these nanofibers using MOR nanocrystals. The nanofibers have shown multilevel pore combinations, such as mesopores and macropores. IR-Py demonstrates the nature type, and desorption strength of the acid sites in the ANF-HMOR, which prevail between 423 and 673 K. The methanol dehydration reactions showed the advantage of the ANF-HMOR synergistically contributing to increase methanol conversion and DME selectivity.

View Article Online
DOI: 10.1039/D2CY00143H

Acknowledgments

The authors thank Jimmy A.Faria (Catalytic Processes and Materials (CPM), University of Twente) and Mark Smithers (MESA+ Institute, University of Twente) for their support. The research leading to the results in this report has received funding from the European Research Council (ERC) under the European Union's Horizon 2020 research and innovation program (Grant agreement No. 742004). The authors thank the financial support from the Consejo Nacional de Investigaciones Científicas y Técnicas (CONICET) PIP-2021-11220200100731CO. The authors also thank the Mexican Council for Science and Technology (CONACyT) for funding R.N.Cruz-Herbert postgraduate studies at UANL (932067).

View Article Online
DOI: 10.1039/D2CY00143H

References

1 S. Kiatphuengporn, A. Junkaew, C. Luadthong, S. Thongratkaew, C. Yimsukanan, S. Songtawee, T. Butburee, P. Khemthong, S. Namuangruk, M. Kunaseth and K. Faungnawakij, *Green Chem.*, 2020, **22**, 8572–8583.

2 X. Xu, H. Zhang, Y. Tong, Y. Sun, X. Fang, J. Xu and X. Wang, *Appl. Surf. Sci.*, 2021, **550**, 149316.

3 L. C. Buelens, V. V. Galvita, H. Poelman, C. Detavernier and G. B. Marin, *Science (80-.).*, 2016, **354**, 449–452.

4 D. Li, Y. Li, X. Liu, Y. Guo, C. W. Pao, J. L. Chen, Y. Hu and Y. Wang, *ACS Catal.*, 2019, **9**, 9671–9682.

5 C. Italiano, J. Llorca, L. Pino, M. Ferraro, V. Antonucci and A. Vita, *Appl. Catal. B Environ.*, 2020, **264**, 118494.

6 H. Jeong, O. Kwon, B. S. Kim, J. Bae, S. Shin, H. E. Kim, J. Kim and H. Lee, *Nat. Catal.*, 2020, **3**, 368–375.

7 J. Ihli, R. R. Jacob, M. Holler, M. Guizar-Sicairos, A. Diaz, J. C. Da Silva, D. Ferreira Sanchez, F. Krumeich, D. Grolimund, M. Taddei, W. C. Cheng, Y. Shu, A. Menzel and J. A. Van Bokhoven, *Nat. Commun.*, 2017, **8**, 1–10.

8 J. L. Williams, *Catal. Today*, 2001, **69**, 3–9.

9 I. Levin and D. Brandon, *J. Am. Ceram. Soc.*, 1998, **81**, 1995–2012.

10 G. Busca, *Catal. Today*, 2014, **226**, 2–13.

11 B. Kasprzyk-hordern, 2004, **110**, 19–48.

12 J. Ruiz and C. Jimenez-Sanchidrian, *Curr. Org. Chem.*, 2007, **11**, 1113–1125.

13 Z. Wang, T. Li, Y. Jiang, O. Lafon, Z. Liu, J. Trébosc, A. Baiker, J. P. Amoureux and J. Huang, *Nat. Commun.*, 2020, **11**, 1–9.

14 K. Motokura, M. Tada and Y. Iwasawa, *J. Am. Chem. Soc.*, 2007, **129**, 9540–9541.

15 B. Dhokale, A. Susarrey-Arce, A. Pekkari, A. Runemark, K. Moth-Poulsen, C. Langhammer, H. Härelind, M. Busch, M. Vandichel and H. Sundén, *ChemCatChem*, 2020, **12**, 6344–6355.

16 Z. Zhang, R. W. Hicks, T. R. Pauly and T. J. Pinnavaia, *J. Am. Chem. Soc.*, 2002, **124**, 1592–1593.

17 P. Euzen, P. Raybaud, X. Krokidis, H. Toulhoat, J.-L. Le Loarer, J.-P. Jolivet and C. Froidefond, *Handb. Porous Solids*.

18 C. Morterra and G. Magnacca, *Catal. Today*, 1996, **27**, 497–532.

19 J. M. McHale, A. Auroux, A. J. Perrotta and A. Navrotsky, *Science (80-.).*, 1997, **277**, 788–789.

20 M. D. Argyle, K. Chen, A. T. Bell and E. Iglesia, *J. Catal.*, 2002, **208**, 139–149.

21 X. Bokhimi, J. Sánchez-Valente and F. Pedraza, *J. Solid State Chem.*, 2002, **166**, 182–190.

22 G. Li, L. Hu and J. M. Hill, *Appl. Catal. A Gen.*, 2006, **301**, 16–24.

23 C. Márquez-Alvarez, N. Žilková, J. Pérez-Pariente and J. Čejka, *Catal. Rev. - Sci. Eng.*, 2008, **50**, 222–286.

24 F. Rascón, R. Wischert and C. Copéret, *Chem. Sci.*, 2011, **2**, 1449–1456.

25 C. Parra-Cabrera, C. Achille, S. Kuhn and R. Ameloot, *Chem. Soc. Rev.*, 2018, **47**, 209–230.

26 S. Danaci, L. Protasova, V. Middelkoop, N. Ray, M. Jouve, A. Bengaouer and P. Marty, *React. Chem. Eng.*, 2019, **4**, 1318–1330.

27 A. Mahapatra, B. G. Mishra and G. Hota, *Ceram. Int.*, 2011, **37**, 2329–2333.

28 C. Weidmann, K. Brezesinski, C. Suchomski, K. Tropp, N. Grosser, J. Haetge, B. M. Smarsly and T. Brezesinski, *Chem. Mater.*, 2012, **24**, 486–494.

29 X. Yang, C. Shao and Y. Liu, *J. Mater. Sci.*, 2007, **42**, 8470–8472.

30 A. F. Lotus, R. K. Feaver, L. A. Britton, E. T. Bender, D. A. Perhay, N. Stojilovic, R. D. Ramsier and G. G. Chase, *Mater. Sci. Eng. B Solid-State Mater. Adv. Technol.*, 2010, **167**, 55–59.

31 A. F. Lotus, Y. C. Kang, J. I. Walker, R. D. Ramsier and G. G. Chase, 2010, **166**, 61–66.

32 A. M. Azad, *Mater. Sci. Eng. A*, 2006, **435–436**, 468–473.

33 W. Fu, Y. Dai, J. P. H. Li, Z. Liu, Y. Yang, Y. Sun, Y. Huang, R. Ma, L. Zhang and Y. Sun, *ACS Appl. Mater. Interfaces*, 2017, **9**, 21258–21266.

34 X. Meng, W. Xu, Z. Li, J. Yang, J. Zhao, X. Zou, Y. Sun and Y. Dai, *Adv. Fiber Mater.*, 2020, **2**, 93–104.

35 H. Dai, J. Gong, H. Kim and D. Lee, *Nanotechnology*, 2002, **13**, 674–677.

36 A. Stanishevsky, W. A. Brayer, P. Pokorny, T. Kalous and D. Lukáš, *Ceram. Int.*, 2016, **42**, 17154–17161.

37 A. H. Hekmati, A. Rashidi, R. Ghazisaeidi and J. Y. Drean, *Text. Res. J.*, 2013, **83**, 1452–1466.

38 R. Jaeger, H. Schönherr and G. J. Vancso, *Macromolecules*, 1996, **29**, 7634–7636.

View Article Online
DOI: 10.1039/D2CY00143H

562 39 J. Doshi and D. H. Reneker, *J. Electrostat.*, 1995, **35**, 151–160.

563 40 M. Tebyetekerwa and S. Ramakrishna, *Matter*, 2020, **2**, 279–283.

564 41 S. Cavaliere, S. Subianto, I. Savych, D. J. Jones and J. Rozière, *Energy Environ. Sci.*,
565 2011, 4, 4761–4785.

566 42 C. Eyovge, C. S. Deenen, F. Ruiz-Zepeda, S. Bartling, Y. Smirnov, M. Morales-Masis,
567 A. Susarrey-Arce and H. Gardeniers, *ACS Appl. Nano Mater.*, 2021, **4**, 8600–8610.

568 43 M. A. Rodriguez-Olguin, H. Atia, M. Bosco, A. Aguirre, R. Eckelt, E. D. Asuquo, M.
569 Vandichel, J. G. E. Gardeniers and A. Susarrey-Arce, *J. Catal.*, 2022, **405**, 520–533.

570 44 P. K. Panda, *Trans. Indian Ceram. Soc.*, 2007, **66**, 65–76.

571 45 X. Tang and Y. Yu, *Ceram. Int.*, 2015, **41**, 9232–9238.

572 46 J. Chandradass and M. Balasubramanian, *J. Mater. Process. Technol.*, 2006, **173**, 275–
573 280.

574 47 R. Nass and H. Schmidt, *J. Non. Cryst. Solids*, 1990, **121**, 329–333.

575 48 L. Ji, J. Lin, K. L. Tan and H. C. Zeng, *Chem. Mater.*, 2000, **12**, 931–939.

576 49 T. F. Baumann, A. E. Gash, S. C. Chinn, A. M. Sawvel, R. S. Maxwell and J. H.
577 Satcher, *Chem. Mater.*, 2005, **17**, 395–401.

578 50 L. Zhang, J. C. C. Chan, H. Eckert, G. Helsch, L. P. Hoyer and G. H. Frischat, *Chem.*
579 *Mater.*, 2003, **15**, 2702–2710.

580 51 S. Rezgui and B. C. Gates, *Chem. Mater.*, 2002, **6**, 2386–2389.

581 52 X. Y. Yang, G. Tian, L. H. Chen, Y. Li, J. C. Rooke, Y. X. Wei, Z. M. Liu, Z. Deng,
582 G. Van Tendeloo and B. L. Su, *Chem. – A Eur. J.*, 2011, **17**, 14987–14995.

53 S. Mitchell, A. B. Pinar, J. Kenvin, P. Crivelli, J. Kärger and J. Pérez-Ramírez, *Nat. Commun. 2015 61*, 2015, **6**, 1–14.

54 A. Susarrey-Arce, M. A. Hernández-Espinosa, F. Rojas-González, C. Reed, V. Petranovskii and A. Licea, *Part. Part. Syst. Charact.*, 2010, **27**, 100–111.

55 T. Li, J. Ihli, Z. Ma, F. Krumeich and J. A. Van Bokhoven, *J. Phys. Chem. C*, 2019, **123**, 8793–8801.

56 J. Di, H. Chen, X. Wang, Y. Zhao, L. Jiang, J. Yu and R. Xu, *Chem. Mater.*, 2008, **20**, 3543–3545.

57 S. F. Anis, A. Khalil, Saepurahman, G. Singaravel and R. Hashaikeh, *Microporous Mesoporous Mater.*, 2016, **236**, 176–192.

58 S. F. Anis and R. Hashaikeh, *Microporous Mesoporous Mater.*, 2016, **233**, 78–86.

59 S. F. Anis, G. Singaravel and R. Hashaikeh, *RSC Adv.*, 2018, **8**, 16703–16715.

60 J. Liu, G. Jiang, Y. Liu, J. Di, Y. Wang, Z. Zhao, Q. Sun, C. Xu, J. Gao, A. Duan, J. Liu, Y. Wei, Y. Zhao and L. Jiang, *Sci. Reports 2014 41*, 2014, **4**, 1–6.

61 S. Ivanova, B. Louis, M. J. Ledoux and C. Pham-Huu, *J. Am. Chem. Soc.*, 2007, **129**, 3383–3391.

62 S. Gao, X. Wang and W. Chu, *Microporous Mesoporous Mater.*, 2012, **159**, 105–110.

63 F. Ocampo, H. S. Yun, M. M. Pereira, J. P. Tessonnier and B. Louis, *Cryst. Growth Des.*, 2009, **9**, 3721–3729.

64 P. Losch, M. Boltz, K. Soukup, I. H. Song, H. S. Yun and B. Louis, *Microporous Mesoporous Mater.*, 2014, **188**, 99–107.

65 C. Pham-Huu, G. Winé, J. P. Tessonnier, M. J. Ledoux, S. Rigolet and C. Marichal,

View Article Online
DOI: 10.1039/D2CY00143H

Carbon N. Y., 2004, **42**, 1941–1946.

66 X. Ke, X. Zhang, H. Liu, S. Xue and H. Zhu, *Chem. Commun.*, 2013, **49**, 9866–9868.

67 I. Hussain, A. A. Jalil, N. S. Hassan, H. U. Hambali and N. W. C. Jusoh, *Chem. Eng. Sci.*, 2020, **228**, 115978.

68 Y. Tao, H. Kanoh, L. Abrams and K. Kaneko, *Chem. Rev.*, 2006, **106**, 896–910.

69 Hamed Bateni and Chad Able, *Catal. Ind.*, 2019, **11**, 7–33.

70 J. Sun, G. Yang, Y. Yoneyama and N. Tsubaki, *ACS Catal.*, 2014, **4**, 3346–3356.

71 S. R. Blaszkowski and R. A. Van Santen, *J. Am. Chem. Soc.*, 1996, **118**, 5152–5153.

72 J. J. Spivey, *Chem. Eng. Commun.*, 1991, **110**, 123–142.

73 M. Ravi, V. L. Sushkevich and J. A. van Bokhoven, *Chem. Sci.*, 2021, **12**, 4094–4103.

74 Z. Cheng, S. Huang, Y. Li, K. Cai, Y. Wang, M. Wang, J. Lv and X. Ma, *ACS Catal.*, 2021, **11**, 5647–5657.

75 I. Takahara, M. Saito, M. Inaba and K. Murata, *Catal. Lett. 2005 1053*, 2005, **105**, 249–252.

76 F. Yaripour, F. Baghaei, I. Schmidt and J. Perregaard, *Catal. Commun.*, 2005, **6**, 147–152.

77 M. Ghavipour and R. M. Behbahani, *J. Ind. Eng. Chem.*, 2014, **20**, 1942–1951.

78 D. Liu, C. Yao, J. Zhang, D. Fang and D. Chen, *Fuel*, 2011, **90**, 1738–1742.

79 A. I. Osman, J. K. Abu-Dahrieh, D. W. Rooney, S. A. Halawy, M. A. Mohamed and A. Abdelkader, *Appl. Catal. B Environ.*, 2012, **127**, 307–315.

80 K. C. Tokay, T. Dogu and G. Dogu, *Chem. Eng. J.*, 2012, **184**, 278–285.

81 S. S. Akarmazyan, P. Panagiotopoulou, A. Kambolis, C. Papadopoulou and D. I. Kondarides, *Appl. Catal. B Environ.*, 2014, **145**, 136–148.

82 J. F. DeWilde, H. Chiang, D. A. Hickman, C. R. Ho and A. Bhan, *ACS Catal.*, 2013, **3**, 798–807.

83 M. A. Christiansen, G. Mpourmpakis and D. G. Vlachos, *ACS Catal.*, 2013, **3**, 1965–1975.

84 S. R. Matkovic, M. Bosco, S. E. Collins and L. E. Briand, *Appl. Surf. Sci.*, 2019, **495**, 143565.

85 J. Aguado, D. P. Serrano, J. M. Escola and A. Peral, *J. Anal. Appl. Pyrolysis*, 2009, **85**, 352–358.

86 H. M. Lankapati, D. R. Lathiya, L. Choudhary, A. K. Dalai and K. C. Maheria, *ChemistrySelect*, 2020, **5**, 1193–1198.

87 P. Intarapong, S. Iangthanarat, P. Phanthong, A. Luengnaruemitchai and S. Jai-In, *J. Energy Chem.*, 2013, **22**, 690–700.

88 R. Cuevas-garcía, J. G. Téllez-romero, J. Ramírez, P. Sarabia-bañuelos and I. Puente-lee, *Catal. Today*, 2021, **360**, 63–71.

89 M. Dyballa, U. Obenaus, M. Blum and W. Dai, *Catal. Sci. Technol.*, 2018, **8**, 4440–4449.

90 M. Dyballa, D. K. Pappas, E. Borfecchia, P. Beato, U. Olsbye, K. P. Lillerud, B. Arstad and S. Svelle, *Microporous Mesoporous Mater.*, 2018, **265**, 112–122.

91 K. S. W. Sing, D. H. Everett, R. A. W. Haul, L. Moscou, R. A. Pierotti, J. Rouquerol and T. Siemieniewska, *Pure Appl. Chem.*, 1985, **57**, 603–619.

92 F. Hosseinzadeh and H. Sarpoolaky, *J. Inorg. Organomet. Polym. Mater.*, 2019, **29**, 1956–1971.

93 V. Antochshuk, M. Kruk and M. Jaroniec, *J. Phys. Chem. B*, 2003, **107**, 11900–11906.

94 K. M. S. Khalil, *J. Colloid Interface Sci.*, 2007, **307**, 172–180.

95 P. Zhu, P. Tian, Y. Liu, H. Pang, W. Gong, J. Ye and G. Ning, *Microporous Mesoporous Mater.*, 2020, **292**, 109752.

96 L. Qu, C. He, Y. Yang, Y. He and Z. Liu, *Mater. Lett.*, 2005, **59**, 4034–4037.

97 J. Aguado, J. M. Escola, M. C. Castro and B. Paredes, *Microporous Mesoporous Mater.*, 2005, **83**, 181–192.

98 E. P. Parry, *J. Catal.*, 1963, **2**, 371–379.

99 A. Piovano, E. Morra, M. Chiesa and E. Groppo, *ACS Catal.*, 2017, **7**, 4915–4921.

100 X. Liu, *J. Phys. Chem. C*, 2008, **112**, 5066–5073.

101 C. A. EMEIS, *ChemInform*, 2010, 24, no-no.

102 M. Tamura, K. I. Shimizu and A. Satsuma, *Appl. Catal. A Gen.*, 2012, **433–434**, 135–145.

103 S. Khabtou, T. Chevreau and J. C. Lavalley, *Microporous Mater.*, 1994, **3**, 133–148.

104 R. J. Mikovsky and J. F. Marshall, *J. Catal.*, 1976, **44**, 170–173.

105 R. Van Borm, A. Aerts, M. F. Reyniers, J. A. Martens and G. B. Marin, *Ind. Eng. Chem. Res.*, 2010, **49**, 6815–6823.

106 M. Xu, J. H. Lunsford, D. W. Goodman and A. Bhattacharyya, *Appl. Catal. A Gen.*, 1997, **149**, 289–301.

669 107 S. M. Kim, Y. J. Lee, J. W. Bae, H. S. Potdar and K. W. Jun, *Appl. Catal. A Gen.*, 2008, **348**, 113–120.

671 108 L. Zeng, Y. Wang, J. Mou, F. Liu, C. Yang, T. Zhao, X. Wang and J. Cao, *Int. J. Hydrogen Energy*, 2020, **45**, 16500–16508.

673